



Synthesis, structural, antimicrobial activity and dielectric properties of Ce³⁺-doped Ni–Zn nano-ferrites

N. Hari kumar^{1,2} · D. Ravinder¹ · Avula Edukondalu^{1,3}

Received: 20 August 2022 / Accepted: 27 September 2022 / Published online: 17 October 2022
© The Author(s), under exclusive licence to Springer-Verlag GmbH, DE part of Springer Nature 2022

Abstract

Citrate-gel auto-combustion was used to create cerium-doped nickel zinc ferrite Ni_{0.2}Zn_{0.8}Ce_xFe_{2-x}O₄ nanoparticles at lower temperatures, where $x = 0.000, 0.020, 0.030, \text{ and } 0.040$. The X-ray diffractometer was used to characterise the powders that were manufactured and sintered. The single-phase cubic spinel structure was validated by XRD samples. The observed results can be analysed and exposed depending on the chemical composition and crystalline size. The nanoparticles' crystalline size (D) ranged from 12.8 to 22.7 nm. The antibacterial efficacy of the created nanocomposites was evaluated using the auger diffusion technique. In this way, this research proposes an $x = 0.00$ to 0.04 nanocomposite that can reduce gram-positive and gram-negative bacterial activity on-demand for pharmaceuticals and medical nanocarriers. The 20 Hz to 2 MHz frequency range and the dielectric characteristics at room temperature were investigated using the LCR bridge. It was possible to generate phase variations in the octahedral sites as well as the hopping mechanism of electrons in the Fe²⁺ and Fe³⁺ ions.

Keywords Synthesis · Nano-ferrites · XRD · Antimicrobial activity · DC dielectric properties

1 Introduction

In the last few decades, researchers have become more interested in the unusual electrical and magnetic properties of cubic spinel ferrites whose general formula is AB₂O₄ [1], where A site (tetrahedral) is occupied by divalent elements such as Ni, Mn, Co, Mg, and Ce, and B site (octahedral) is associated with trivalent metal ions Fe³⁺ [2]. Magnetic spin filters [3], read or write heads for high-speed digital tape, data storage [4], ferro-fluid, electromagnetic shields, magneto-optical devices, magnetic diagnostic equipment, soft magnetic fabrication, power generators, magnetic memory devices, magnetic recording media, air conditioners and phase shifters are just a few of the applications for

ferrites in the electrical industry. Ferrite nanoparticles are employed in hyperthermia treatment of cancers [5], magnetic resonance imaging (MRI) [6], drug targeting [7], catalysis [8] and waste water treatment [9] in biomedical applications. Because of their high permeability [10, 11], ferrites are employed in broad band transformers, antenna rods and electromagnetic wave absorbers in electromagnetic field applications because of their high permeability. Due to their high resistance, ferrite materials are appropriate for use in microwave devices, Curie temperatures and chemical stability. Nano-ferrites are good dielectric materials that are employed at a wide variety of frequencies, from microwave to radio, and have more technical uses in the high frequency region.

Normal and inverse spinel structures are based on the rearrangement of cation distribution in two unique sub-lattices of the A site (tetrahedral) and B site (octahedral) [12, 13]. Ni ferrites and Zn ferrites have radically different properties due to their opposite crystallisation paths; NiFe₂O₄ is ferrimagnetic and ZnFe₂O₄ is anti-ferromagnetic [14]. The calcination and sintering conditions are particularly susceptible to these ferrite characteristics. Because of their magnetic characteristics, easily modulable structure and adequate biocompatibility, Ni–Zn ferrites have received a lot of attention. The Zn²⁺, Fe³⁺ ions and Ni²⁺, Fe³⁺ ions occupied

✉ N. Hari kumar
namaharikumar@gmail.com

✉ D. Ravinder
ravindergupta28@rediffmail.com

¹ Department of Physics, University College of Science, Osmania University, Hyderabad, India

² Dr B.R. Ambedkar College, Baghlingampally, Hyderabad 500044, India

³ Department of Physics, University Post Graduate College, Osmania University, Secunderabad, Telangana 500003, India

octahedral and tetrahedral positions in the cubic spinel structure in Ni–Zn ferrites, which have an inverse spinel structure. At ambient temperature, charge carriers can move between Fe^{2+} and Fe^{3+} ions at the octahedral sites [7]. Because of the displacement of ions in the tetra and octahedral sites, the concentration of Zn has a significant impact on the Ni–Zn ferrites. Furthermore, these ferrites improved the spinel ferrite's intrinsic and extrinsic characteristics. High-frequency Ni–Zn ferrites are employed in high-frequency applications (10–500 MHz) [15].

By altering the heat treatment, calcination, and sintering conditions in nickel-zinc ferrites, the electrical and magnetic properties can be altered. Various authors have prepared mixed Ni–Zn ferrites using a variety of methods, including the auto-combustion chemical method [16], the sol–gel method [17], the co-precipitation method [18], the solid state reaction method [19], the citrate precursor method [20], the microwave sintering method [21], and the poly acrylamide gel method, and reported various properties of Ni–Zn ferrites. Because of its low cost, high homogeneity, good stoichiometry, and influence on the structural, electrical, and magnetic properties of spinel ferrites, auto-combustion was chosen as the preferred approach.

Ni–Zn ferrites doped with rare earth metal cations will have better mechanical, electromagnetic, chemical and physical characteristics. At ambient temperature, the rare earth doped Y– CoFe_2O_4 , Sm– CoFe_2O_4 and Pr– CoFe_2O_4 compounds exhibit high dielectric constant values, according to Samad et al. [22]. Sanpo and his colleagues examined ferrites' biological activity, particularly in terms of bactericidal mechanisms and healing powers. Existing biological features in ferrite nanoparticles can be improved by introducing transition metals [23, 24].

The effects of rare earth doping in metal oxides and spinel structure on switching parameter enhancement and stability were investigated. Wang et al. discovered that the leakage current density was reduced in a five molar percent cerium-replaced BiFeO_3 thin film [25]. Lee et al. investigated cerium doping, which raised the nanoparticle size of the ZrO_2 film and likely reduced the film fault without increasing the total number of O_2 vacancies [26]. Younis et al. discovered resistance switching properties in CeO_2 thin films, co-doped CeO_2 nanorods, and CeO_2 nanotubes [27–29]. Observations by Patil et al. observed that Ce– MgFe_2O_4 was shown to be a viable material for manufacturing high-performance acetone sensors [30]. Nasrabadi et al. investigated cerium-doped CuFe_2O_4 nanoparticles as a photo catalyst for the breakdown of toxic organic dyes [31]. Heiba et al. reported that the rare earth elements doped Ni ferrites have cation distribution and dielectric properties [32]. Elaya Kumar et al. reported that nickel ferrite nanoparticles with cerium content have antibacterial activity when tested on gram-negative and gram-positive bacteria and applications [33].

The electrical characteristics of Ce^{3+} ferrite nanoparticles are critical for electrical and electronic applications. In the present work, we prepared $\text{Ni}_{0.2}\text{Zn}_{0.8}\text{Ce}_x\text{Fe}_{2-x}\text{O}_4$ samples with 0.000, 0.020, 0.030, and 0.040 samples and reported the XRD analysis, antimicrobial activity, and dielectric property.

2 Materials and methods

2.1 Synthesis

The auto-combustion process was used to create the Ce doped Ni–Zn ferrites, which have the chemical formula $\text{Ni}_{0.2}\text{Zn}_{0.8}\text{Ce}_x\text{Fe}_{2-x}\text{O}_4$ (where $x = 0.000, 0.020, 0.030,$ and 0.040), and all the precursors are A.R grade. Nickel nitrate [$\text{Ni}(\text{NO}_3)_2 \cdot 6\text{H}_2\text{O}$], zinc nitrate [$\text{Zn}(\text{NO}_3)_2 \cdot 6\text{H}_2\text{O}$], ferric nitrate [$\text{Fe}(\text{NO}_3)_3 \cdot 9\text{H}_2\text{O}$], citric acid [$(\text{C}_6\text{H}_8\text{O}_7) \cdot \text{H}_2\text{O}$], and cerium nitrate [$\text{Ce}(\text{NO}_3)_3 \cdot 6\text{H}_2\text{O}$] are used as raw materials. The stoichiometric amounts of nitrates were first dissolved in the required quantity of deionized water and later added to the citric acid in the ratio of 1:1 to the solution. The pH of the solution was maintained above seven by adding ammonia (NH_3) drop by drop after raising the temperature of the magnetic agitator from room temperature to 800°C to get the gel form of the solution. After some time, the resulting solution was changed to a viscous gel, and the solution was stirred and heated between 180 and 2000°C , which resulted in burned ash. The collected ash powder was grounded well into powder and heated for 4 h at 500°C in a muffle furnace to remove the volatile compounds and impurities present in the sample. The XRD patterns for all compositions of $\text{Ni}_{0.2}\text{Zn}_{0.8}\text{Ce}_x\text{Fe}_{2-x}\text{O}_4$ (where $x = 0.000, 0.020, 0.030,$ and 0.040) were investigated at room temperature by using a Rigaku Miniflex-600 diffractometer, and anti-microbial studies were conducted to test the gram positive and negative of pathogenic bacteria against plant component extracts. The dielectric constant properties of pure and Ce^{3+} doped Ni–Zn ferrites were measured at frequencies ranging from 2 Hz to 20 MHz. The materials were converted into pellets for AC conductivity tests by adding binder and applying consistent pressure in a hydraulic press. The investigation of AC conductivity allows for a more thorough interpretation of the conduction and mobility charge processes in a fluctuating electric field. An AC electrical conductivity study may help to better understand how electrical polarisation is enhanced. The electrical conductivity of both pure and cerium-doped Ni–Zn ferrite nanoparticles affects frequency variation.

2.2 The antibacterial activity method

The antibacterial activity of cerium-doped Ni–Zn nanoferrite particles was investigated by the auger disc diffusion

method and used to test the gram positive and negative of pathogenic bacteria against plant component extracts for five pathogenic bacteria. Antimicrobial activity testing was done using the auger cup method. Samples that had been synthesised and processed were kept at 4 °C. In this study, to determine the zone of inhibition [39], pure gram-positive and gram-negative strains were used as typical ampicillin antibiotics for assessment of the outcome. The antibacterial activity of all the produced ferrite powders was tested against *Escherichia coli* and *Staphylococcus aureus*. Ferrites and sets of five compounds (30 µg/g) were produced in double-distilled water. At 37 °C for 3 h, the powder was mixed with indicator bacterial strains (108 cfu) in Mueller–Hinton sterile auger plates. After 24 h, the increase in inhibition discs in incubation at 37 °C for bacteria at 28 °C was measured. The inhibitory zones were measured in millimetres.

2.3 Characterization techniques

The XRD pattern was created with a Rigaku Miniflex-600. An Auger diffusion technique was employed to evaluate the antibacterial effectiveness of the created nano-composite. The dielectric constant was measured as real (ϵ') and imaginary (ϵ'') portions at room temperature using an Agilent E4986A Precision LCR meter with frequency dependency ranging from 20 Hz to 2 MHz (Fig. 1).

3 Results and discussions

3.1 XRD analysis

The XRD calculations of the Ce-doped Ni–Zn ferrite nanoparticle peaks are slightly broader and have a lower particle size (nm) as shown in Fig. 2. The present diffraction peaks match with the standard JCPDS: 48-0489, which refers to all the sample peaks belonging to the cubic spinel structure and shows the development of a single-phase structure with the *Fd-3m* space group. The average nanoparticle size in the range of about 12.8–22.7 nm was calculated using Scherrer's formula [34]. Table 1 shows the X-ray density (D_x) and volume of the unit cell of each composition. The lattice parameters were indicated to be increasing to decreasing from 8.46 to 8.39 Å with increasing cerium substitution, but particle size values were increased. Because Ce³⁺ ionic radius has a larger ionic radius (1.03 Å) than Fe³⁺ ionic radius (0.64 Å), so it should take up more space on the B site than the A site, resulting in a decrease in unit cell volume [35]. Hopping lengths " L_A " and " L_B " are used to describe the distance between magnetic ions at tetrahedral sites (A) and octahedral sites (B). The hopping lengths calculated using the formulas $L_A = \frac{a\sqrt{3}}{4}$ and $L_B = \frac{a\sqrt{2}}{4}$ [36] and the dislocation density (ρ_D)

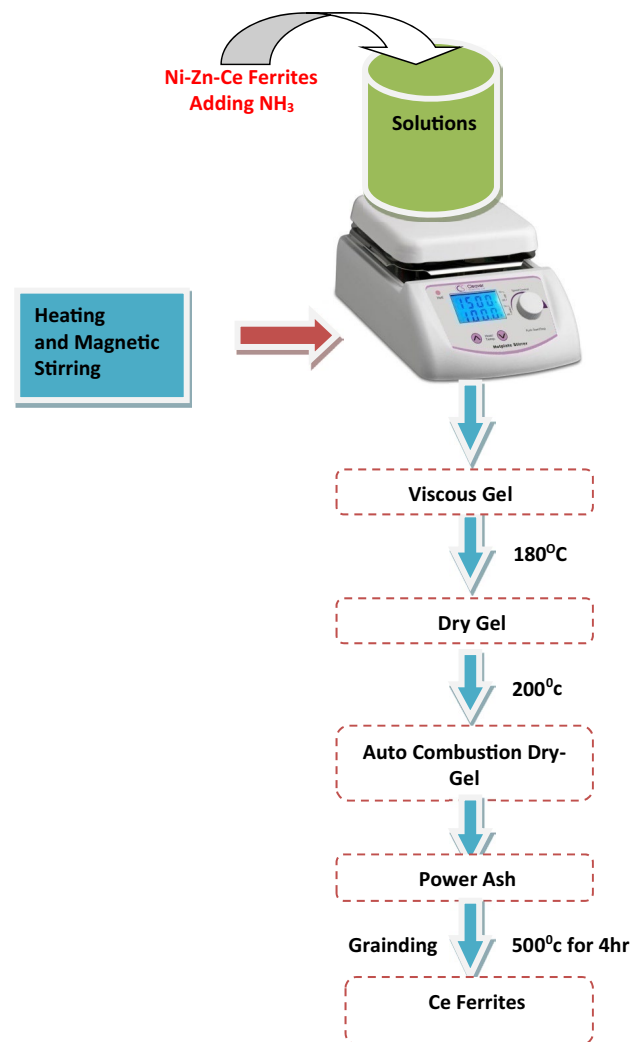


Fig. 1 Synthesis flow chart for nanoparticles

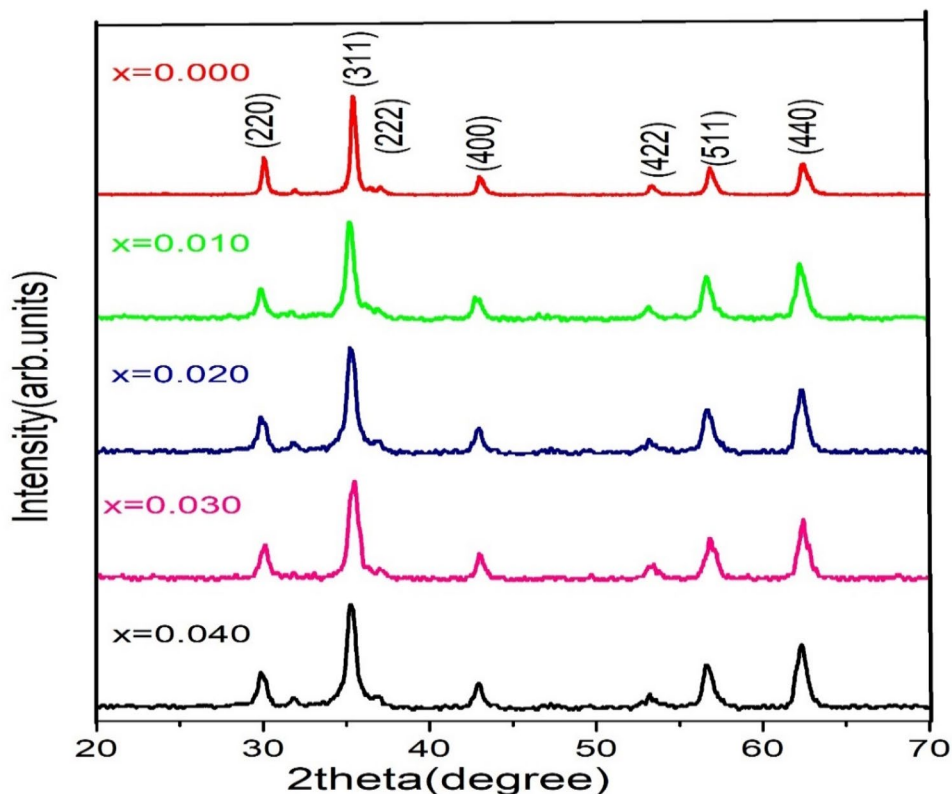
were calculated using the formula $= 1/D^2$, where D is the size of the crystallite. Values are shown in Table 1.

The Williamson–Hall equation, which is used to calculate the average crystallite size (D) and strain (ϵ).

$$\beta \cos \theta = \frac{K\lambda}{D} + 4\epsilon \sin \theta \quad (1)$$

In Fig. 2, the computed values are given, and it can be seen that all of the peaks are noticeable, with the planar fitting being the most prominent. The data from the linear function was evaluated and plotted. The crystallite size and lattice strain were determined using the Y-intercept slope plots [37], as shown in Table 1. Because the ionic radii of Ce³⁺ (1.03 Å) and Fe³⁺ (0.64 Å) ions in the octahedral site are greater than those of Fe³⁺ (0.64 Å), the Cerium doped Ni–Zn ferrite of the lattice strain increased with increasing Cerium content [38]. The difference in crystallite size obtained by XRD using the Debye Scherer formula, as well

Fig. 2 XRD pattern of Ce substituted Ni–Zn nano-ferrites



as the Williamson–Hall relation, are both consistent, and the values and the literature are well aligned (Fig. 3).

3.2 Anti-microbial studies

This work evaluated the antibacterial effectiveness of the $\text{Ni}_{0.2}\text{Zn}_{0.8}\text{Ce}_x\text{Fe}_{2-x}\text{O}_4$ nano-composite against gram-positive and gram-negative bacteria using standard auger diffusion and quantitative growth inhibition methods. The composition of $x=0.000, 0.010, 0.020, 0.030,$ and 0.04 nanocomposite demonstrated strong antibacterial activity against Sol–gel auto-combustion chemical technique by presenting a definite inhibitory zone, as shown in Fig. 4. The inhibitory zones on the nanoparticle impregnated discs were 0.1, 0.5, and 0.1 mm in size, showing that the generated nano-composite had comparable enhanced bacterial activity.

When cerium concentration rises, as in Fig. 4, the antibacterial property is increased because the nanoscale of the generated materials should be reduced, allowing the nanoparticles to more readily enter the cell membrane and inhibit bacterial growth [39–41]. The small-sized nanoparticle’s penetration within the cell wall and subsequent cell damage were thought to be caused by an electrostatic interaction between positively charged nanoparticles and negatively charged bacteria. Due to the significant oxidative damage that reactive oxygen species (ROS) inflict, microorganisms may not be able to grow. Microorganisms may

not be able to develop due to the severe oxidative damage caused by reactive oxygen species (ROS). The cell membrane structure can further deteriorate as a result of this. In $\text{Ni}_{0.2}\text{Zn}_{0.8}\text{Ce}_x\text{Fe}_{2-x}\text{O}_4$, cerium is doped to increase the specific surface area and to create reactive oxygen species, which also alters bacterial growth. The $x=0.040$ sample’s surface area, morphology, and particle size all significantly influence their antibacterial activity.

This is located on the skin, in the nasal passages, and in the respiratory system. Various illnesses, from skin infections to life-threatening disorders, can be brought on by it. It contributes to several infections linked to healthcare. include urethral and pulmonary complications [42, 43].

3.3 Dielectric measurements

3.3.1 Dielectric constant

The dielectric constant of prepared samples $\text{Ni}_{0.2}\text{Zn}_{0.8}\text{Ce}_x\text{Fe}_{2-x}\text{O}_4$ (where $x=0.000, 0.010, 0.020, 0.030$ and 0.040) was studied as a function of real (ϵ') and imaginary (ϵ'') parts at room temperature. The dielectric frequency dependence is in the range of 20 Hz to 2 MHz. Figure 5 displays the dielectric constant’s real (ϵ') and imaginary (ϵ'') parts. Due to the migration of an equivalent number of Fe^{3+} ions from tetrahedral positions to octahedral sites caused by the doping of Ce^{3+} ions, Ce-substituted Ni–Zn nano-ferrite samples

Table 1 The average molecular weight (*M*), crystalline size, lattice parameter, X-ray density and volume, experimental density (*d_p*), crystallite size, strain, hopping lengths (*L_A* and *L_B*) and dislocation density (*ρ_D*) from W–H plots

Composition	<i>M</i> (g/mol)	Crystalline size (nm)	Lattice constant (Å ^o)	<i>(d_x)</i> (gm/cc)	Volume (Å ^o) ³	<i>(d_e)</i> (gm/cc)	Crystalline size <i>D</i> (nm)		Strain	<i>L_A</i> (Å ^o)	<i>L_B</i> (Å ^o)	<i>ρ_D</i>
							W–H	Scherrer formula				
Ni _{0.2} Zn _{0.8} Fe ₂ O ₄	239.73	22.7	8.40	5.35	594.2	3.2	42.20	17.78	0.0030	3.637	2.969	0.0004
Ni _{0.2} Zn _{0.8} Ce _{0.010} Fe _{1.99} O ₄	240.57	18.4	8.46	5.27	605.4	3.5	16.50	13.65	0.0012	3.663	2.990	0.0036
Ni _{0.2} Zn _{0.8} Ce _{0.020} Fe _{1.98} O ₄	241.42	19.3	8.45	5.30	603.3	3.6	13.72	13	0.0040	3.658	2.987	0.0053
Ni _{0.2} Zn _{0.8} Ce _{0.030} Fe _{1.97} O ₄	242.26	12.8	8.39	5.43	590.5	3.9	15.75	12.20	0.0016	3.632	2.965	0.0040
Ni _{0.2} Zn _{0.8} Ce _{0.040} Fe _{1.96} O ₄	243.10	19.3	8.42	5.39	596.9	4.0	15.57	12.13	0.0015	3.645	2.976	0.0041

exhibit greater dielectric constant values at lower frequencies, as seen in the graph. Because of this, the dielectric constant is increased at octahedral sites by electron hopping between Fe²⁺ and Fe³⁺ ions. Murugesan et al. [44] discovered similar high dielectric constant behaviour in Gd³⁺ substituted cobalt ferrite. But drops as the frequency increases, indicating region independence at higher frequencies [45]. Because of the substituted rare earth Ce³⁺ ions, which have higher ionic radii than Ni and Fe ions [46], and the dielectric constant is affected by particle size as well [47]. The particle size has an increasing trend from the W–H plots. When the particle size increases, the dielectric constant decreases, so it is affection for the doped Ce³⁺ metal ion. Their low levels are caused by the inhibition of the transfer of electrons between ferric and ferrous ions, which results in less polarisation [48]. The imaginary (*ε''*) part of the dielectric constant is represented by a steep curve with an initial frequency of 20 Hz to 2 MHz, and the curve gradually diminishes as the frequency increases. In Koop's theoretical model [49], it is presupposed that the dielectric ferrite structure is made up of a layer that conducts electricity very well-made up of grains and a layer that conducts electricity very poorly composed of grain boundaries. It is well known that grains themselves exhibit more efficacy at high frequencies, whereas grain borders exhibit greater effectiveness [46]. At low frequencies, polarisation results in a high value of the dielectric constant. This behaviour is consistent with the Maxwell–Wagner type space charge polarization, which is supported by Koop's phenomenological theory [50]. Table 2 provides the real and imaginable values of the dielectric constant.

3.3.2 AC conductivity

The electrical properties were studied through the AC conductivity is the major study in materials, which measures the conductivity of the sample itself. Since the same element's ions were present in many valence states, the ferrites' conductivity resulted from the movement of electrons between these ions. To determine the AC conductivity (*σ_{AC}*) of the prepared Cerium doped Ni–Zn ferrites for all samples with frequency ranges from 20 Hz to 2 MHz at room temperature, it's shown in Fig. 6.

From Fig. 5, it can be observed that the AC conductivity of the samples exhibited almost independent behaviour at low frequencies and after, gradually increasing with increasing of frequency. Maxwell–Wagner and Koop's phenomenologist theory [51] were explored in similar ways. Due to the increased activity of grain boundaries at lower frequencies and the diminished hopping mechanism of Fe²⁺ and Fe³⁺ ions, the conductivity is low. From Table 2, at the higher frequencies, the AC conductivity values are found to increase from 2.50 × 10⁶ to 2.72 × 10⁶ Ω⁻¹ cm⁻¹ with the doping concentration of Cerium. M.A. Almessiere et al. [52] found similar

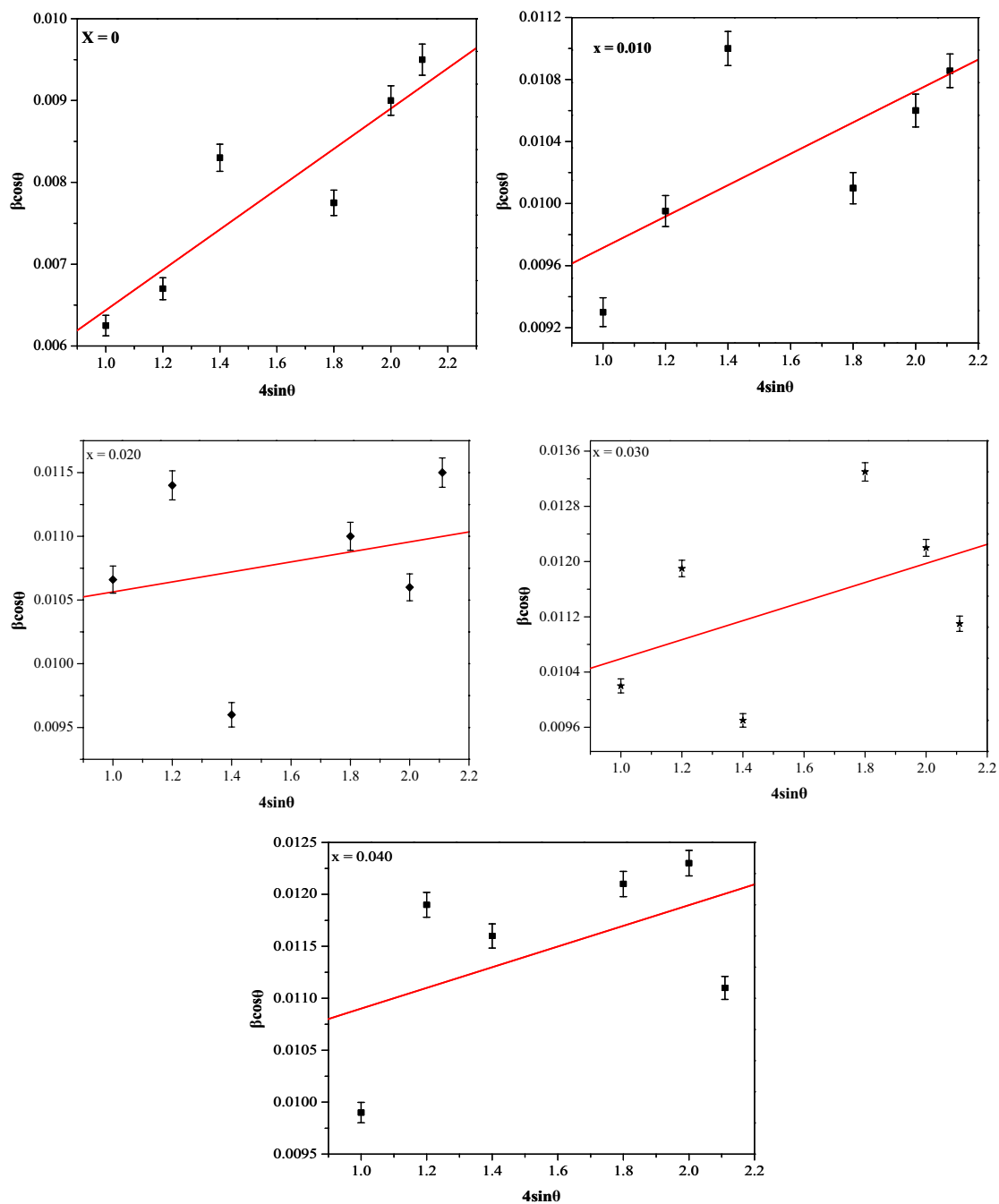


Fig. 3 W–H plots of $\text{Ni}_{0.2}\text{Zn}_{0.8}\text{Ce}_x\text{Fe}_{2-x}\text{O}_4$ (where $x=0.000$ to 0.040 with step of 0.010)

types of results for $\text{Ni}_{0.5}\text{Co}_{0.5}\text{Ce}_x\text{Dy}_x\text{Fe}_{2-2x}\text{O}_4$ ($x \leq 0.10$) with increasing the frequency for all temperatures and with composition. The conductivity of the sample grain borders becomes less active as the applied field is increased, and the hopping of ion contacts is quite high. The conductivity increases linearly with frequency, confirming the polaron type of conduction. However, the composition of $x=0.000$ is unique; it follows the other composition criteria. Due to the Scherrer relation, the crystallite size is large compared to the doped materials.

The electrical AC conductivity at room temperature, the ferrites' lower value compositions show, may be advantageous for microwave applications with minor eddy current losses benefit [53].

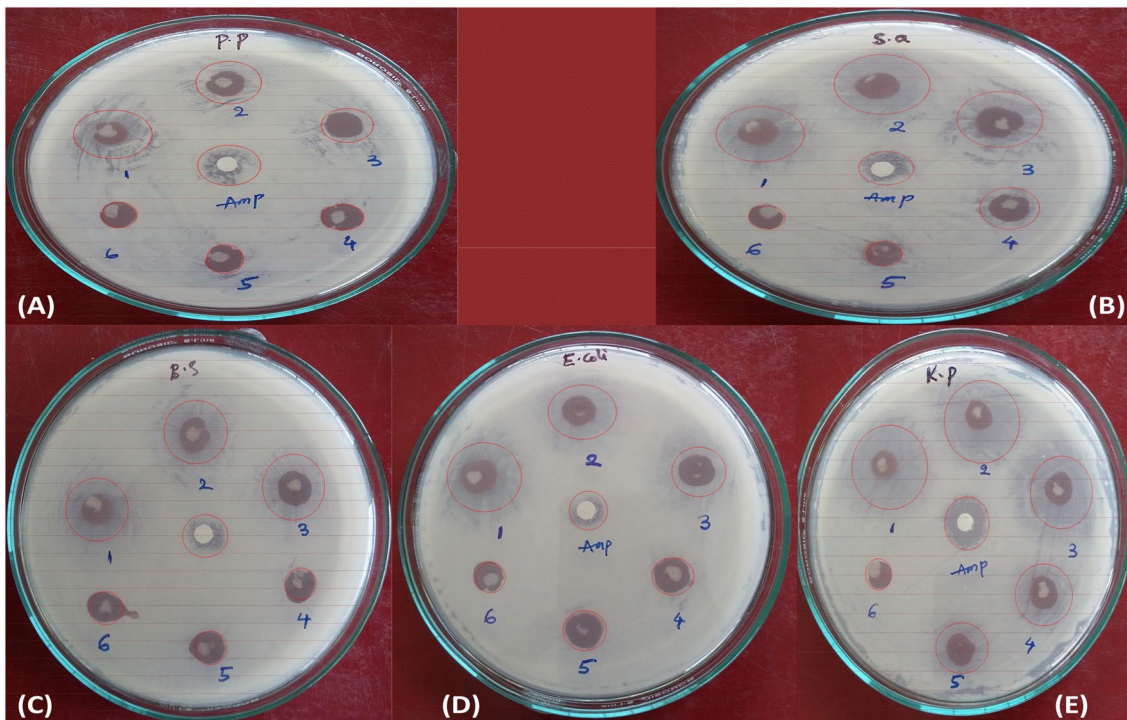


Fig. 4 The zone of inhibition of as a control and the Ni_{0.2}Zn_{0.8}Ce_xFe_{2-x}O₄ nano-composite nanoparticle and, water-suspended nanoparticles in an against where x=0.000 to 0.040 with step of 0.010 bacterial using the agar diffusion method

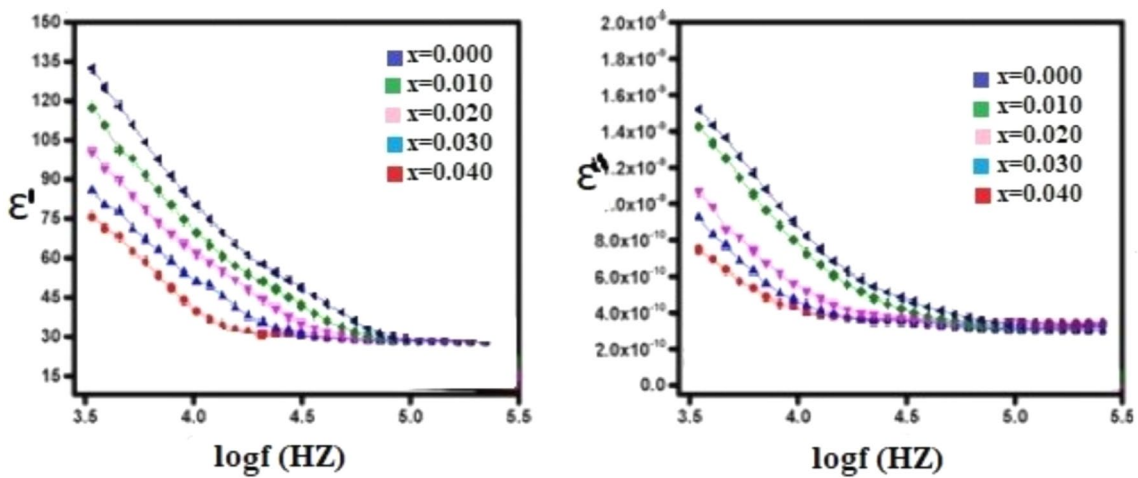
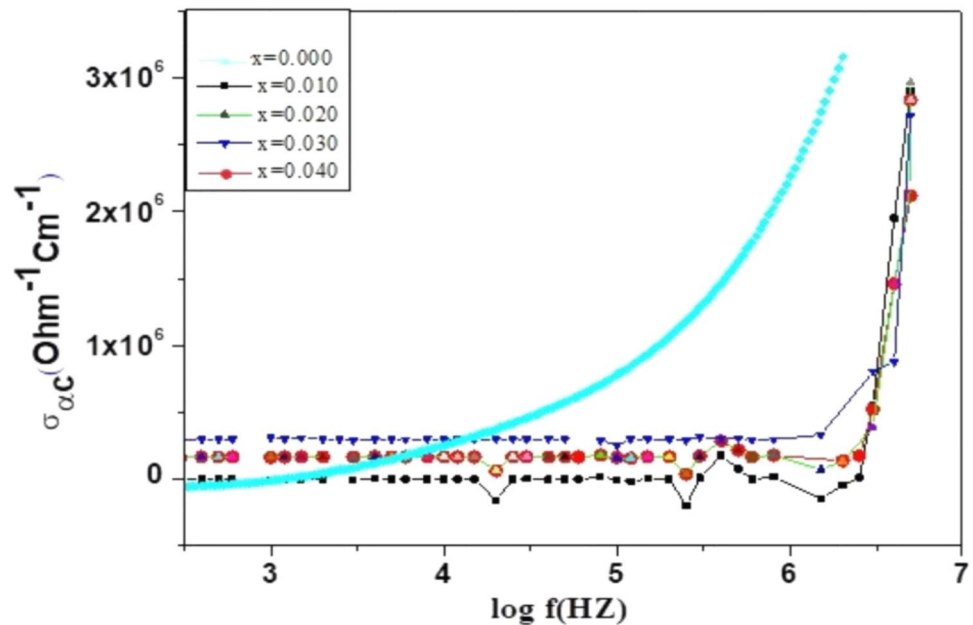


Fig. 5 Variation of real and imaginary parts of dielectric constant with frequency of Ni_{0.2}Zn_{0.8}Ce_xFe_{2-x}O₄ (where x=0.000 to 0.040 with step of 0.010)

Table 2 Variation in dielectric constant real and imaginary and AC conductivity of Ni_{0.2}Zn_{0.8}Ce_xFe_{2-x}O₄

Composition	Dielectric constant real (ε') (Hz)	Dielectric constant imaginary (ε'') (Hz)	AC conductivity (σ _{AC})×10 ⁶
Ni _{0.2} Zn _{0.8} Fe ₂ O ₄	79.3	1.84	2.72
Ni _{0.2} Zn _{0.8} Ce _{0.010} Fe _{1.99} O ₄	55.64	2.83	2.90
Ni _{0.2} Zn _{0.8} Ce _{0.020} Fe _{1.98} O ₄	30.26	1.92	2.61
Ni _{0.2} Zn _{0.8} Ce _{0.030} Fe _{1.97} O ₄	15.21	1.48	2.43
Ni _{0.2} Zn _{0.8} Ce _{0.040} Fe _{1.96} O ₄	9.084	1.02	2.50

Fig. 6 Variation of ac conductivity with frequency of $\text{Ni}_{0.2}\text{Zn}_{0.8}\text{Ce}_x\text{Fe}_{2-x}\text{O}_4$ (where $x=0.000$ to 0.040 with step of 0.010)



4 Conclusions

In this current work, the ferrite compositions $\text{Ni}_{0.2}\text{Zn}_{0.8}\text{Ce}_x\text{Fe}_{2-x}\text{O}_4$ (where $x=0.0, 0.01, 0.02, 0.03,$ and 0.04) were synthesised through the citrate gel-auto-combustion method, and the crystallite size was between 12.8 and 22.7 nm. The W–H plot method was used to calculate the crystallite size and strain to compare with the Scherrer equation. The prepared samples were tested using standard auger diffusion and quantitative growth inhibition methods. Cerium dopant was found to be more effective as an antibacterial agent against *Staphylococcus aureus* than *Klebsiella pneumoniae*. The dielectric constant of all samples is shown to have higher values (79.3–15 Hz) at lower frequencies and independent behaviour at higher frequencies. The reason for this trend is electron hopping. The AC conductivity values are increasing at higher frequencies from 2.50×10^6 to $2.72 \times 10^6 \Omega^{-1} \text{cm}^{-1}$ with the doping concentration of Cerium. The conductivity is low because hopping of Fe^{2+} and Fe^{3+} ions occurs less often at lower frequencies and grain boundaries are more active at those frequencies. These types of materials can be used in high frequency applications because of the reduction of dielectric constant values.

Declarations

Conflict of interest The authors declare that they have no known competing financial interests or personal relationships that could have appeared to influence the work reported in this paper.

References

1. N. Boda, G. Boda, K. Chandra babu Naidu, M. Srinivas, K.M. Batoo, D. Ravinder, A. Panasa Reddy, J. Magn. Magn. Mater **49**, 6501 (2019)
2. A. Aakash, A. RoyChowdhury, D. Das, S. Mukherjee, Ceram. Int. **42**, 6 (2016)
3. A.V. Ramos, Phys. Rev. B **78**, 180402 (2008)
4. S.E. Shirsath, X. Liu, M.H.N. Assadi, A. Younis, Y. Yasukawa, S.K. Karan, J. Zhang, J. Kim, D. Wang, A. Morisako, Y. Yamauchi, S. Li, Nanoscale Horiz. **4**, 434 (2019)
5. M.I.A. Maksoud, S.G. El-Sayyad, A.H. Ashour, A.I. El-Batal, M.S. Abd-Elmonem, H.A.M. Hendawy, E.K. Abdel-Khalek, S. Labib, E. Abdeltwab, M.M. El-Okr, Mater. Sci. Eng. **97**, 27 (2018)
6. A. Gangwar, S.K. Alla, M. Srivastava, S.S. Meena, E.V. Prasadrao, R.K. Mandal, S.M. Yusuf, N.K. Prasad, J. Magn. Magn Mater. **7**, 056727 (2016)
7. R. Ghosh, L. Pradhan, Y. Priyabala Devi, S.S. Meena, A. Kumar, S. Sharma, N.S. Gajbhiye, R.K. Vatsa, B.N. Pandey, R.S. Ningthoujam, J. Mater. Chem. **21**, 13388 (2011)
8. A.M. Banerjee, M.R. Pai, S.S. Meena, A.K. Tripathi, S.R. Bhara-dwaj, Int. J. Hydrog. Energy **36**, 8 (2011)
9. K.K. Kefeni, B.B. Mamba, Sustain. Mater. Technol. **23**, 140 (2020)
10. S. Verma, P.A. Joy, S. Kurian, J. Alloy. Compd. **509**, 37 (2011)
11. I. Ismail, M. Hashim, K.A. Matori, R. Alias, J. Hassan, J. Magn. Magn. Mater. **324**, 2463 (2012)
12. Ch. Sujatha, J. Phys. Chem. Solids **74**(7), 917 (2013)
13. S.I. Ahmad, S.A. Ansari, D. Ravi Kumar, Mater Chem. Phys. **208**, 248 (2018)
14. L. Andjelkovića, M. Suljagićb, M. Lakićc, D. Jeremićc, P. Vulićd, A.S. Nikolichb, Ceram. Int. **44**, 14163 (2018)
15. K.L. Routray, S. Saha, D. Behera, Mater. Chem. Phys. **224**, 29 (2019)
16. A.S. Dzunuzovic, J. Magn. Magn. Mater. **374**, 245 (2015)
17. S. Zahi, M. Hashim, A.R. Daud, J. Magn. Magn. Mater. **308**, 177 (2007)

18. T. Jahanbin, M. Hashim, K.A. Matori, S.B. Waje, J. Alloys Compd. **503**, 1 (2010)
19. C.A. Palacio Gómez, C.A. Barrero Meneses, A. Matute, Mater Sci. Eng. B Solid-State Mater. Adv. Technol. **15**, 1 (2018)
20. A. Verma, T.C. Goel, M.I. Mendiratta Alam, Mater Sci. Eng. B **60**, 156 (1999)
21. M. Sorescu, L. Diamandescu, R. Pelemedu, R. Roy, P. Yadoji, J. Magn. Magn. Mater. **279**, 2 (2016)
22. R. Samad, M. DinRathar, K. Asokan, Basha Asokan, Appl. Phys. A **125**, 8 (2019)
23. N. Sanpo, C.C. Berndt, C. Wen, J. Wang, Acta Biomater. **9**, 5830 (2013)
24. V. Gopinath, S. Priyadarshini, M.F. Loke, J. Arunkumar, E. Marsili, D. MubarakAli, P. Velusamy, J. Vadivelu, Arab. J. Chem. **10**, 1107 (2017)
25. X. Wang, H. Liu, B. Yan, J. Eur. Ceram. Soc. **J. 29**, 1183 (2009)
26. Myung Soo Lee, Sungho Choi, Chee-Hong An, Hyoungsub Ki. Appl. Phys. Lett. **100**, 143504 (2012)
27. A. Younis, D. Chu, S. Li, J. Phys. D Appl. Phys. **45**, 35 (2012)
28. A. Younis, D. Chu, X. Lin, J. Lee, S. Li, Nanoscale Res. Lett. **8**(1), 36 (2013)
29. A. Younis, D. Chu, I. Mihail, S. Li, A.C.S. Appl. Mater. Interfaces **5**, 19 (2013)
30. J.Y. Patil, D.Y. Nadargi, I.S. Mulla, S.S. Suryavanshi, Heliyon **5**, 6 (2019)
31. M. Rahimi-Nasrabadi, M. Behpour, A. Sobhani-Nasa, Mansoureh Rangraz Jed. J Mater Sci: Mater Electron **9**, 2 (2019)
32. Z.K. Heiba, M.B. Mohamed, M.A. Ahmed, M.A.A. Moussa, H.H. Hamdeh, Alloys Compd. **586**, 773 (2014)
33. K. Elaya kumar, V. Sathana, R.T. Kumar, J. Supercond. Nov. Magn. **33**, 2171–2178 (2020)
34. N. Hari Kumar, D. Ravinder, T. Anil Babu, N. Venkatesh, S. Swathi, N.V. Krishna Prasad, J. Indian Chem. Soc. **99**, 3 (2022)
35. S.M. Hosseinpour-Mashkani, A. Sobhani-Nasab, M. Maddahfar, J. Nanostruct **6**(1), 67 (2016)
36. M.P. Ghosh, S. Mukherjee, J. Mater. Sci. Mater. Electron. **31**, 8 (2019)
37. J.S. Patila, U.B. Chanshetti, C.B. Pawar, Orient. J. Chem. **38**, 1 (2022)
38. A. Sattar, H.M. El-Sayed, K.M. El-Shokrofy, M.M. El-Tabey, J. Mater. Sci. **5**(1), 162 (2005)
39. Y.S. Khadar, A. Balamurugan, V.P. Devarajan, R. Subramanian, S.D. Kumar, J. Mater. Res. Technol. **8**, 267–274 (2019)
40. Y.A.N.G. Xiaojun, Y.A.N.G. Zhimin, M.A. Changhui, D.U. Jun, Rare Met. **25**, 250 (2006)
41. B. Yalcin, S. Ozcelik, K. Icin, J Mater Sci **32**, 13068–13080 (2021)
42. F.N. Almajhdi, H. Fouad, K.A. Khalil, H.M. Awad, S.H. Mohamed, T. Elsarnagawy, A.M. Albarrag, F.F. Al-Jassir, H.S. Abdo, J. Mater. Sci. Mater. Med. **25**(4), 1045–1053 (2014)
43. H.K. Abdelhakim, E. El-Sayed, F.B. Rashidi, J. Appl. Microbiol. **128**, 6 (2020)
44. C. Murugesan, G. Chandrasekaran, RSC Adv. **10**, 1039 (2015)
45. E.S.R. El-Sayed, H.K. Abdelhakim, Z. Zakaria, Mater. Sci. Eng. C **107**, 11 (2020)
46. D.R. Kumar, C. Abraham Lincoln, D. Ravinder, S.I. Ahmad, J. Appl. Phys. A **126**, 705 (2020)
47. R.C. Kambale, K.M. Song, Y.S. Koo, N. Hur, J. Appl. Phys. A **110**, 053910 (2011)
48. S. Ul, K. Kumar, G. Murugesan, S. Kalainathan, J. Alloys Compd. **701**, 612–618 (2017)
49. C. Murugesan, G. Chandrasekaran, RSC Adv. **5**, 73714 (2015)
50. C.G. Koops, Phys. Rev. **83**, 121 (1951)
51. K.M. Batoo, Phys. B Condens. Matter **406**, 382 (2011)
52. M.A. Almessiere, B. Unal, Y. Slimani, H. Gungunes, M.S. Toprak, N. Tashkandi, A. Baykal, M. Sertko, A.V. Trukhanov, A. Yıldız, A. Manikandan, J. Mater. Res. Technol **14**, 2534–2553 (2021)
53. M.A. Elkestawy, J. Alloys Compd. **492**, 616 (2010)

Publisher's Note Springer Nature remains neutral with regard to jurisdictional claims in published maps and institutional affiliations.

Springer Nature or its licensor holds exclusive rights to this article under a publishing agreement with the author(s) or other rightsholder(s); author self-archiving of the accepted manuscript version of this article is solely governed by the terms of such publishing agreement and applicable law.